Core Origin of Seismic Velocity Anomalies at the Earth's Core-Mantle Boundary

- Suyu Fu^{1,3,*}, Stella Chariton², Vitali B. Prakapenka², and Sang-Heon Shim^{1,*}
- ⁴ School of Earth and Space Exploration, Arizona State University, Tempe, Arizona, USA.
- ⁵ Center for Advanced Radiation Sources, University of Chicago, Chicago, Illinois, USA.
- ⁶ Now at Department of Earth and Planetary Science, The University of Tokyo, Tokyo, Japan.
- *fsyxhy@gmail.com; sshim5@asu.edu

Seismic studies have found fine-scale anomalies at the core-mantle boundary (CMB), such as ultralow velocity zones (ULVZs)^{1,2} and the core rigidity zone (CRZ)^{3,4}. ULVZs have been attributed to mantle-related processes⁵⁻¹⁰, but little is known about possible core origin. Precipitation of light elements in the outer core has been proposed to explain the CRZ^3 , but it remains unclear what processes can lead to such precipitation. Despite the importance of silicon and hydrogen in the outer core¹¹, constraints on the melting behaviour of Fe-Si-H at relevant pressure-temperature conditions are still lacking. Here, we report experimental observations of crystallization of a B2-structured Si-rich FeSi alloy from Fe-9wt%Si (9 wt% Si) melted in the presence of hydrogen up to 125 GPa and 3700 K using laser-heated diamond anvil cells. We found that hydrogen dramatically increases the Si concentration in the B2 crystals (Si/Fe \approx 1), while it mostly remains in the coexisting Fe liquid. The 17 high Si content in the B2 phase makes it stable in a solid form at the outermost-core temperatures and less dense than the surrounding liquids. Consequently, the Si-rich crystallites could form, float, 19 and be sedimented to the underside of the CMB interface, and that well explains the core-side rigidity anomalies^{3,4}. If a small amount (8.4 vol%) of the FeSi crystals can be incorporated into the 21 mantle under convection flow, they would form dense low-velocity structures above the CMB, which may account for some ULVZs¹⁰. The B2 FeSi precipitation promoted by H in the outermost core 23 provides a single core-driven origin for two types of anomalies at the CMB. Such a scenario could 24 also explain the core-like tungsten isotope signatures in ocean island basalts¹², after the materials equilibrated with the precipitates are entrained to the uppermost mantle by the mantle plumes rooting at ULVZs.

Introduction

The Earth's core-mantle boundary (CMB) represents an interface between the solid silicate mantle and the liquid metallic outer core, and structure and dynamics in this region are fundamental for understanding heat and material transfer in our planet¹¹. Fine-scale seismic velocity anomalies have been detected at the CMB, such as the ultra-low velocity zones (ULVZs)^{1,2} and the core rigidity zone (CRZ)³. ULVZs exist at the base of the mantle^{1,2} with thicknesses of 3–100 km, compressional and shear wave velocity reductions of up to 25% and 50%, respectively, and density increases of 5–20%. The observed CRZ is less than 2–km thick at the core side near CMB, allows for the propagation of shear waves, and displays a density decrease of <40% compared to the surrounding liquid outermost core³.

A range of models have been proposed to explain the origin of ULVZs, including partial melt¹³ or iron-

enriched materials (i.e., post-perovskite⁷, magnesiowüstites⁸, FeSi alloys¹⁰, and hydrogen-bearing Fe peroxide⁹) in the mantle and/or via subduction into the CMB region⁶. Buffet et al.¹⁴ also proposed that reactions between mantle and core materials may produce silicate sediments at the top of the Earth's core. While many of these involve mantle processes, the role of the core has not been considered as much. On the other hand, the CRZ has been attributed to possible precipitation of light elements in the liquid outermost core³. However, it is not known what light elements are being incorporated into such precipitates and what factors can result in such crystallization.

The Earth's core consists of Fe-Ni alloys with a few percent of light elements¹¹, including Si, H, S, O, and C. Among them, of particular interest are Si and H due to their abundances¹⁵ and high solubilities in Fe metal at high pressure-temperature (P-T) conditions^{16,17}. Studies have estimated as much as 10 wt% Si and 1 wt% H in the outer core^{11,18}. However, experimental datasets for the melting behaviours of Fe-Si-H ternary system^{19–22} are limited to 62 GPa and 3000 K.

Here, we report a series of high *P-T* experiments where a pure H₂ or Ar-H₂ mixture was used as a H source to react with Fe-Si alloys with 9 wt% Si (Fe-9wt%Si; Fe_{0.83}Si_{0.17}) up to 125 GPa and 3700 K in laser-heated diamond anvil cells (LHDACs) (see Extended Data Figure 1 for experimental setup). Use of an Ar-H₂ mixture limits the amount of H (less than 1.7 wt%) to the metal alloy, unlike a pure H₂ source (see Methods). It also significantly reduces H diffusion to diamond anvils, decreasing the likelihood of diamond breakage and enabling high-temperature heating relevant to the liquid outer core for a longer duration. Furthermore, unlike paraffin (C_nH_n) or water as a H source, an Ar-H₂ mixture medium prevents participation of other elements in the reaction, effectively isolating factors controlling chemical processes. Synchrotron X-ray diffraction (XRD) measurements were conducted on the heated spots at in-situ high *P-T* and after temperature quench. These characterizations allow us to understand the Si partitioning between metal alloy melts and solids, as well as crystallization of the Fe-Si-H ternary. Our results provide key data to link core processes with seismologically observed velocity anomalies at the CMB region^{1,3}.

2 Results

After laser heating the Fe-9wt%Si starting material to 2400–3700 K at 49.5–124.8 GPa (Extended Data Figure 3, Extended Data Table 1, and Methods), optical images of the sample show the removal of metal alloy at the heated center where the transparent hydrogen fills the space (Figure 1 insert). Such a signature was not found when the sample was heated to sub-solidus temperatures. Before heating, the Ar-H₂ mixture forms $Ar(H_2)_2$ at 300 K and high pressures²³. The diffraction peaks of $Ar(H_2)_2$ are mostly replaced by Ar diffraction lines after heating, indicating that Ar(H₂)₂ breaks down and releases H₂ at high temperatures, 68 which subsequently reacts with the starting Fe-9wt%Si. Therefore, the convection of the medium, which should be molten at high temperatures, likely removed some of the liquid metal alloy, resulting in the 70 observed optical texture. XRD patterns on the heated area after temperature quench show that the melting 71 of Fe-9wt%Si in H produces face centered cubic (fcc) FeH_x, double hexagonal close-packed (dhcp) FeH_x, 72 and B2 $\text{Fe}_{1-\delta}\text{Si}_{1+\delta}$ (δ for Si deviation from Si/Fe = 1; Figure 1). We also observed a small amount 73 of the cubic FeH₃ (space group: $Pm\bar{3}m$) after heating above 100 GPa, which is likely frozen melt with 74 local enrichment of H. Early experiments¹⁹ reported the synthesis of H-bearing hcp Fe-6.5 wt%Si phase (1.2–1.5 wt% H) at temperatures below 1000 K at 27–67 GPa. The different phases we observed here 76 likely result from melting. A recent study²² reported the melting behaviour of Fe-Si-H at \sim 50 GPa, which 77 is far lower than the pressure expected for the outer core.

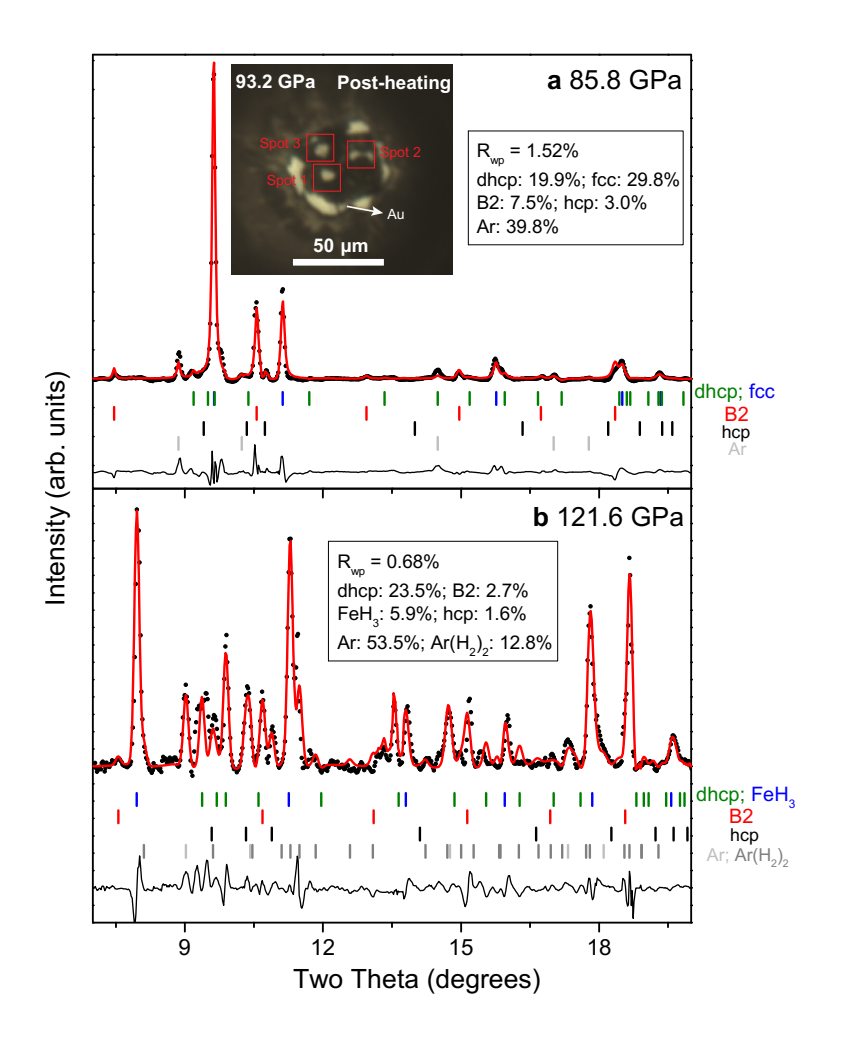


Figure 1. Rietveld refinements of the X-ray diffraction patterns collected after the melting of Fe-9wt%Si in a H-bearing medium **a** at 85.8 GPa and 3400 K and **b** at 121.6 GPa and 3300 K. The black circles are measured intensities, the red curves are the best fits, and the black curves are residuals. Peak positions of different phases are shown in the coloured vertical ticks: dhcp FeH_x (red), fcc FeH_x or cubic FeH₃ (blue), B2 FeSi (orange), and a small amount of a hcp phase (black). Ar and Ar(H₂)₂ from the pressure medium were labeled as light gray and gray ticks, respectively. Residue factor (R_{wp}) and mole fractions of phases were provided in the legend. The wavelength of incident X-ray beam is 0.3344 Å. The insert in **a** shows an optical image of the sample after heating at 93.2 GPa. The red rectangles indicate three molten spots up to 3400 K.

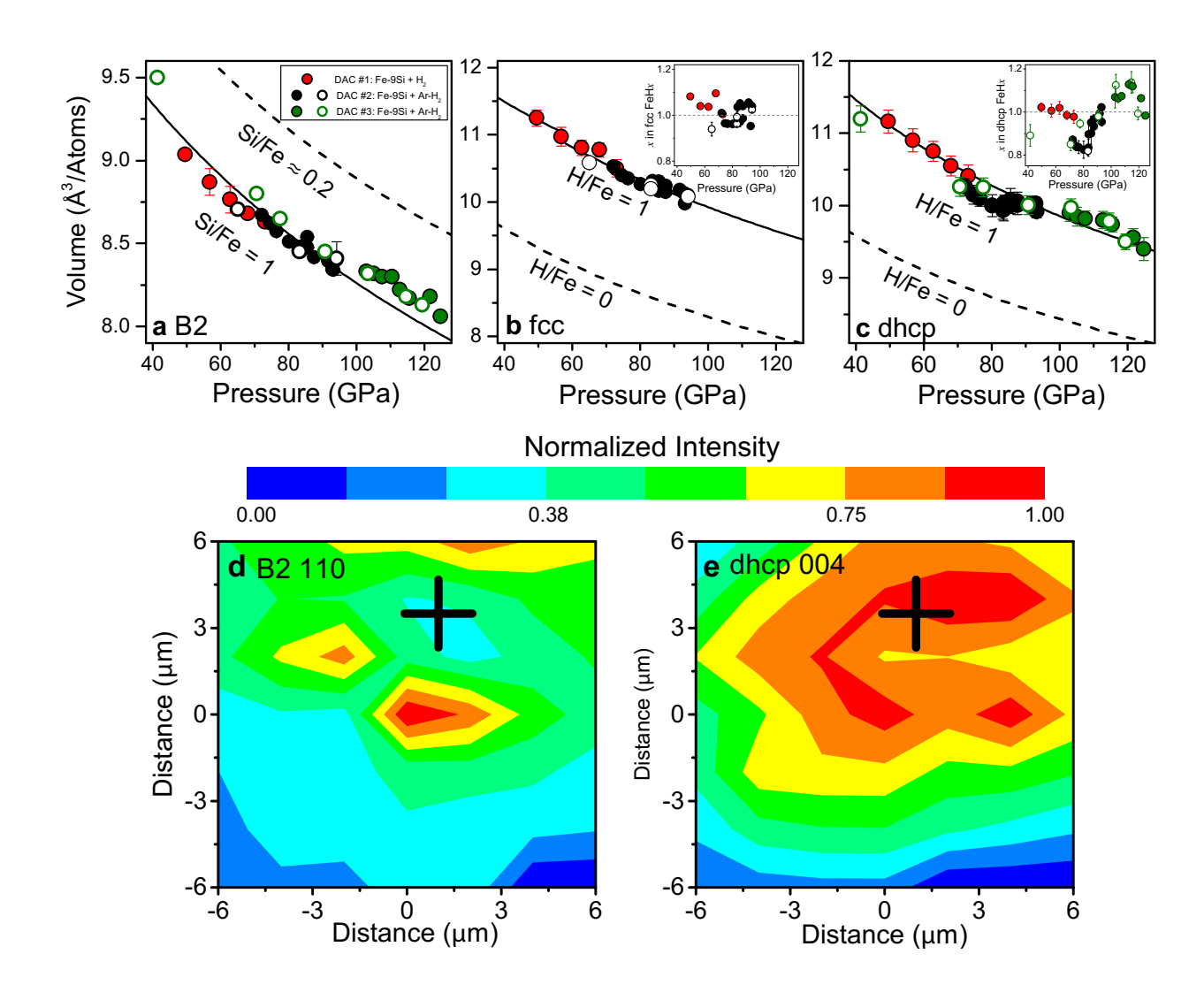


Figure 2. Characterization of the temperature quenched samples. **a-c** Composition estimations of the phases observed after laser heating at 300 K using the measured volumes. **a** B2 FeSi, **b** fcc FeH_x, and **c** dhcp FeH_x. The red, black, and olive circles are from different samples (DACs #1, #2, and #3). The solid and open circles are measured volumes during compression and decompression, respectively. Previous experimental reports on B2 FeSi¹⁶, D0₃ Fe-9wt%Si¹⁶, fcc FeH²⁴, and dhcp FeH¹⁷ were plotted as solid curves for comparison. **d-e** Two-dimensional distribution of the phases in the heated region at 102.9 GPa after heating to 3300 K. **d** B2 110 diffraction peak, **e** dhcp 004 diffraction peak. The contours are normalized intensities of the selected peaks. The crosses mark the heating center. Much more FeH_x exists at the heating center while more B2 FeSi exists around the hottest spot. This texture indicates that FeH_x is the quenched liquid, while B2 FeSi is the first crystallizing phase during temperature quench.

The effects of H and Si on the volumes of Fe alloy phases 16,17,24 are well known at high pressures and 300 K, which can be used to estimate compositions of the temperature-quenched products in this study (Extended Data Table 2 and see Methods). This method is particularly effective in the case of the sample synthesized in a H or Ar-H₂ medium because the heated sample foils are severely mechanically weakened 82 from fracturing by the convection of the molten medium and are therefore difficult to recover for chemical 83 analysis at 1 bar. The volumes of the B2 phase show slight deviations (< 1.3%) from those of H-free B2 FeSi phase¹⁶ (Figure 2a). A recent study²⁰ found about 0.1 wt% H in B2 FeSi with a 2% volume decrease. Therefore, the observed volume decreases below 70 GPa in this study can be attributed to 86 0.06 wt% H in the B2 structure. As to the $\sim 1.3\%$ volume increase in the B2 structure above 100 GPa, based 87 on the existing data of the Si effect on the volume of B2 Fe-Si alloys 16, we attribute it to a slight deviation of the Si content from Si/Fe = 1 by less than ± 0.05 . Considering the minimal Si or H deviations from FeSi in the B2 phase, we will use FeSi for its composition in the rest of this paper. The observed volumes of fcc and dhcp phases match well with those of FeH_x alloys 17,24 with H/Fe ≈ 1 (Figure 2b-c). The slightly 91 smaller volumes of the dhcp phase at 72–84 GPa might be attributed to a relatively low H/Fe ratio (>0.8). However, we do not rule out the possibility of other effects, such as a spin or magnetic transition²⁵. Above 100 GPa, we observed a small amount of cubic FeH₃ (6 mol% from Rietveld refinements) (Figure 1b). The pressure range of the observation is consistent with an earlier report ¹⁷. The cubic phase displays a 95 4–5% higher volume than pure FeH₃ ¹⁷ (Extended Data Figure 4a). The slight increase in volume can be from more H or a small amount of Si in the phase. As Fe liquid may have a larger H solubility²⁶, we interpret that the observed FeH₃ in this study formed from a local H enrichment during the temperature quench. We also found a small amount (<3 mol%) of remnant hcp phase after heating (Extended Data 99 Figure 4b and see Supplementary Information).

Two-dimensional XRD maps of the heated areas show that more FeH_x exists near the heated center, while more B2 FeSi exists at the edge (Figure 2d-e). The FeH_x-rich area is 3–4 μ m away from the hotspot center due to the removal of metal alloy at the highest temperature region (Figure 1a insert), as well as the limited $(2-\mu m)$ spatial resolution in XRD mapping. Partial melting of Fe alloys typically resulted in melt at the hot center with coexisting solid phases at the lower-temperature surroundings in LHDACs experiments^{27,28}. The heating temperatures in this study are lower than the melting of FeSi alloy²⁹ and pure Fe metal³⁰ (Extended Data Figure 3). However, the temperatures are higher than the melting temperature of FeH_x alloy³¹, which is approximately 2300 K at 125 GPa, indicating partial melting in our experiments. Given 3900 K for eutectic melting of H-free Fe-Si system²⁷ at \sim 120 GPa, our results show that H greatly reduces the eutectic temperature. The high-temperature XRD patterns show that the solid B2 phase appears when the starting material was heated above \sim 1950 K at 72.2 GPa without any peaks attributable to the fcc or dhcp FeH_x phases (Extended Data Figure 5). It suggests that H is in Fe liquid while crystallites are rich in Si. Therefore, the composition of our starting Fe-9wt%Si alloy should be located at the Si-richer side of the eutectic point (the orange coloured areas in the pseudo-binary sections of Figure 3a). Both high-temperature XRD patterns and 2D XRD maps are consistent with our interpretation that the FeH_x is the quenched H-rich metal melt while B2 FeSi crystallizes first from the liquid during cooling. This observation was consistently made in our experimental runs.

101

102

103

104

105

107

108

109

110

111

112

113

114

115

116

117

In a H-free Fe-Si system²⁷, the Si content in the eutectic liquid decreases from 5.5 wt% at 70 GPa to 2.2 wt% at 120 GPa (Extended Data Figure 6 and the red circle in Figure 3a). Based on our observations discussed above, H further decreases the Si/Fe of the eutectic composition close to 0 at about 120 GPa (Figure 3a). The B2 phase coexisting with melt is reported to have Si/Fe = 0.08-0.22 in a H-free Fe-Si system²⁷, which is far lower than that, \sim 1, when H is present in this study. Although the exact eutectic

composition of the Fe-FeH binary at 120 GPa remains uncertain, our experiments reveal that B2 FeSi would precipitate and the coexisting Fe liquid would be rich in H, if the outer core contains Si at least greater than that expected for the Fe-FeSi eutectic composition²⁷ (2.2 wt% Si) and a few tenth to 1.7 wt% H (see Methods and Figure 3a). As shown in Figure 3a, comparison with the low-pressure study²² indicates that pressure shifts the cotectic lines toward Si-poor side of the ternary diagram.

Discussion

129

130

131

132

133

134

135

137

138

139

141

143

144

145

147

149

150

151

152

153

155

157

158

159

160

161

162

163

Our experiments show that hydrogen can make significant changes in the crystallization behaviour of Fe-Si system. The most notable change is that the B2 phase crystallized from a Fe-Si-H system with a Si content reasonable for the outer core¹¹ has much more Si (Si/Fe \approx 1) than the H-free case²⁷. Among the candidate light elements in the outer core, Si is shown to decrease the melting temperature of Fe alloys the least^{16,31,32,37}. Particularly, Si-rich B2 FeSi displays a comparable or even slightly higher melting temperature than pure Fe metal^{29,30}. As shown in Figure 3b, within the temperature range (3900–4300 K) expected for the present-day outermost core^{30,33,38}, Si-rich B2 FeSi should be stable as a solid because of its high melting temperature, and therefore precipitate. In other words, the first light element that begins to crystallize from a (Si,H)-bearing Earth's outer core by secular cooling would be Si. Because the slope of the B2 FeSi melting curve decreases with pressure²⁹ (Figure 3b), the crystallization of FeSi is likely limited to the topmost region of the outer core. We note that Si should be initially incorporated into the liquid outer core in the early Earth because of its higher temperature than the melting curve of B2 FeSi.

The density of the Si-rich B2 FeSi alloy¹⁶ is as much as 10-20% lower than those of dhcp/fcc FeH_x alloys^{17,24} and hcp Fe metal³⁴ at the outermost core P-T conditions (Figure 3c). Theoretical calculations show that Fe alloy liquids are 1-2% less dense than their solid counterparts³⁶. Therefore, Si-rich B2 FeSi crystallites are approximately 14% less dense than the density of the outermost core³⁵. As a result, the Si-rich B2 FeSi crystallized in a H-bearing liquid outer core would float and be deposited at the CMB (Figure 4). An earlier study suggested that FeSi and FeO could form via reactions of lower-mantle bridgmanite with the core Fe liquid⁵. Our finding here provides a new mechanism, that FeSi forms solely from the cooling of the liquid outer core.

The formation of Si-rich B2 FeSi crystals at the outermost core can have important implications for the origin of seismic velocity anomalies in this region. For instance, a thin CRZ (120–180 m) was found underside the mantle with a detectable shear velocity of 0.6–0.8 km/s and a density reduction of as much as 10-40% compared to the surroundings³. Our model predicts that the B2 FeSi sedimentation is global and therefore a thin B2 FeSi layer forms beneath the CMB (Figure 4). The lateral extension of CRZ is uncertain in seismology because of the small thickness of CRZ close to the detection limit. If a 100-m thin global FeSi layer forms by the FeSi precipitation in a top 40-km thin region of the outer core, it requires a decrease of 0.07 wt% Si in the top 40-km region (see Methods). The 14.4% lower density of B2 FeSi than the surrounding outermost core in the PREM model³⁵ is reasonable for the expected density contrast at the CRZ^{3,4}, 10-40%. The shear velocity of solid B2 FeSi is 5.22 ± 0.07 km/s at the outermost core P-T condition 10 higher than the estimation for the CRZ 3 , 0.6-0.8 km/s. However, if the CRZ is porous and contains some amount of liquid Fe alloy in the pore space¹⁴, the shear velocity can be much lower than that of the pure B2 FeSi solid. In this case, the Si reduction from the outermost core estimated here may be an upper limit. The precipitation of Si-rich solids in the outermost core will consequently make the remaining surrounding liquid slightly denser. The denser melt may sink to the deeper core and the upwelling flow will supply relatively Si-richer melt to the outermost region to prevent radial Si gradient. If

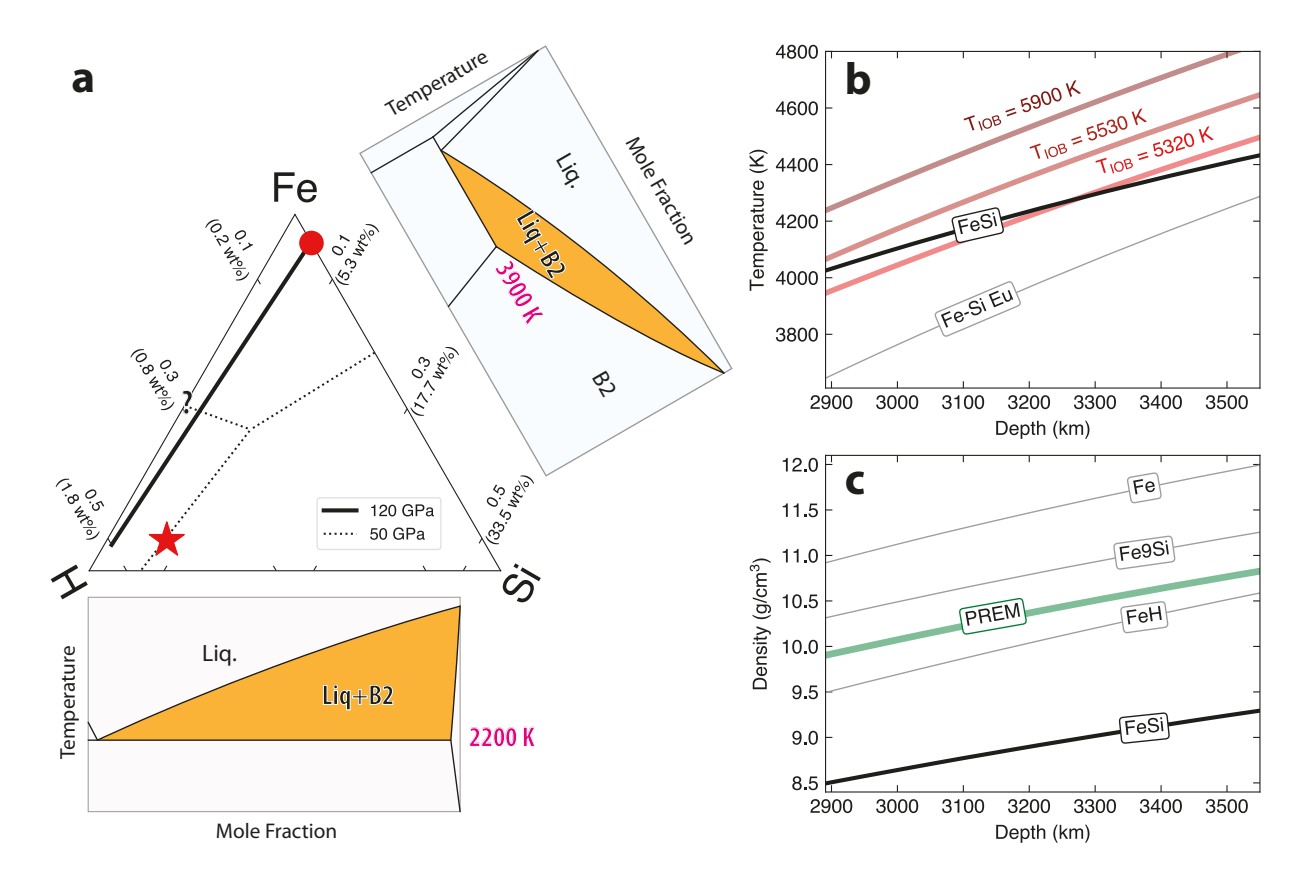


Figure 3. Crystallization of B2 FeSi from the Fe-Si-H system at high P-T. **a** A provisional Fe-Si-H ternary diagram at \sim 120 GPa (solid line). Estimated bulk chemical composition of our Fe-Si-H system is shown by a red star. The eutectic composition is obtained from Ref.²⁷ for a H-free Fe-FeSi system (red circle). The ternary phase relation²² reported at \sim 50 GPa is shown as dashed lines for comparison. The Fe-H eutectic at 120 GPa is not well known and therefore denoted by a question mark. Binary sections for Fe-FeSi²⁷ and FeH-FeSi (this study) are shown for highlighting the hydrogen effect. The axes are in mole fractions with corresponding wt% in parentheses (left axis in H content and right axis in Si content). **b** Melting curves of Fe-Si alloys at the topmost outer core. We show the melting curve of B2 FeSi²⁹ (black) and the solidus temperature of Fe-Si alloys containing 7–22 wt% Si (Fe-Si Eu; gray)³². We include three candidate outer-core geotherms^{30,33} for the temperatures at the inner core boundary ($T_{\rm IOB}$) of 5900, 5530, and 5320 K. **c** The densities of the Earth's outer core candidate Fe alloys along an expected geotherm³⁰: thick black for B2 FeSi¹⁶, and gray for hcp Fe³⁴, hcp Fe-9wt%Si¹⁶, and dhcp FeH¹⁷. Seismic density profile is plotted as a light green curve (PREM)³⁵. Note that these profiles are for solid phases as the thermoelastic properties of these liquid phases are not well known. For liquids, the density may be slightly smaller by 1–2% than solids, according to theoretical calculations³⁶.

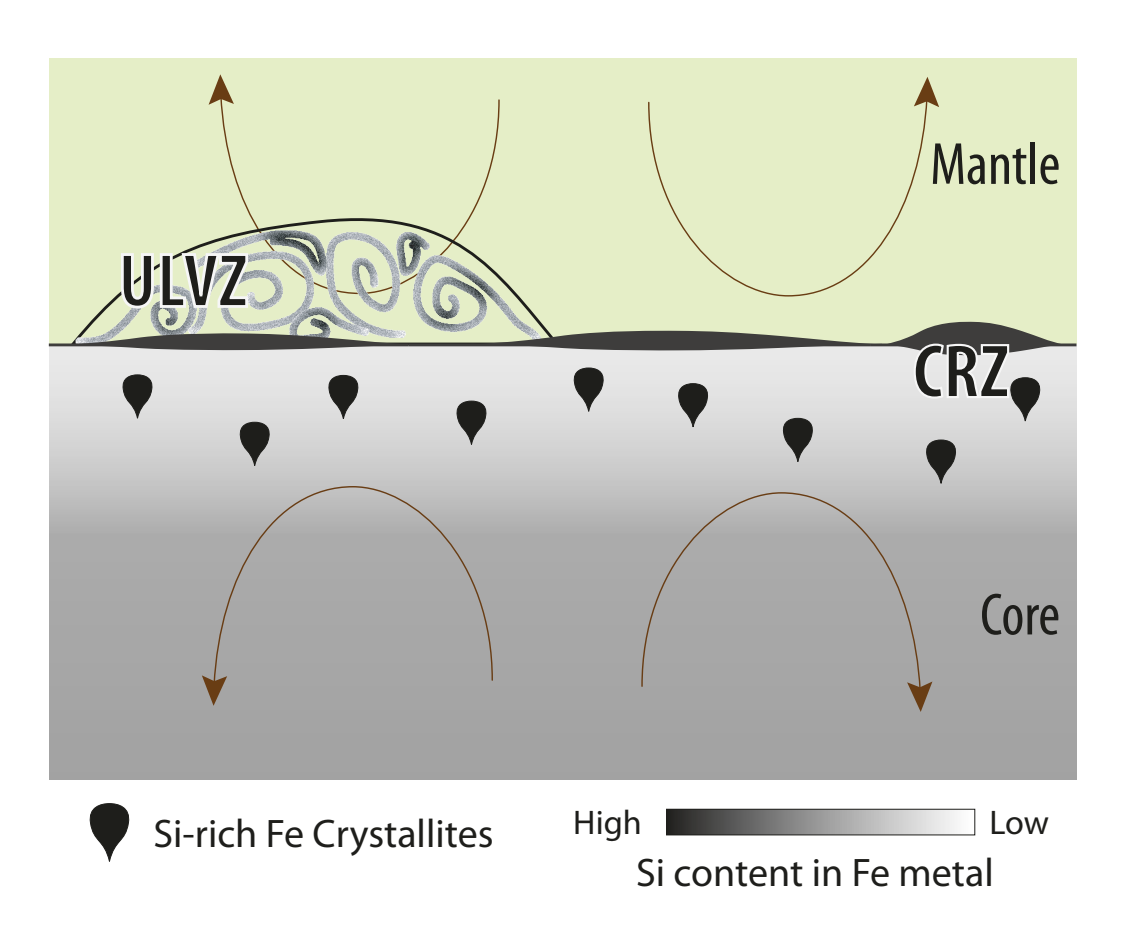


Figure 4. A schematic diagram for the origin of seismologically observed velocity anomalies at the core-mantle boundary. Si as B2 FeSi is likely the first light element to crystallize at the outermost core with secular cooling due to its high melting temperature (Figure 3b). The lower density of the FeSi crystals than the surrounding liquid outer core makes them float and possibly aggregate at the CMB to form the core-rigidity zone (CRZ) at the core side and some ultralow-velocity zones (ULVZs) at the mantle side.

the outer core is well mixed such that the Si loss at the outermost region is compensated by Si-richer Fe metal liquid from the deeper region, the amount of Si loss decreases to 0.003 wt% for the entire outer core (see Methods).

The FeSi crystallized from the outer core has a density 50% higher than that of the lowermost mantle at 168 the CMB. If a small amount of FeSi was swept into the mantle flow and mixed with the lower-mantle silicate minerals (Figure 4), this can contribute to the seismic anomalies at the mantle side of the CMB, 170 such as ULVZs. Although such a high-density contrast may require a sufficiently long time for the B2 FeSi 171 crystallites to mix well with the surrounding mantle³⁹, exsolution of FeSi in a small grain size may dilute 172 the patches and make the mixing possible. A recent seismic study estimated that the detected ULVZs takes up $\sim 10.3\%$ of the CMB globally². An experimental study has shown that less than 8.4 vol\% FeSi in the 174 aggregates can explain both the velocity reduction and the density increase estimated for ULVZs¹⁰. To 175 account for the properties of ULVZs¹⁰ with thicknesses of 10–30 km, 0.06–0.18 wt% Si is required to 176 crystallize in a top 40-km thick region of the liquid outer core (see Methods). If the outer core is well 177 mixed, the Si loss for the entire outer core is 0.003-0.009 wt% to account for ULVZs. Therefore, the 178 required amount of Si is much smaller than the possible Si content in the outer core¹¹, up to 10 wt%. If a 179 range of mechanisms can form ULVZs instead of a single process^{2,40}, the required amount of the core Si 180 loss for ULVZs is even smaller. Overall, our results suggest that the crystallization of solid B2 FeSi at the 181 outermost region of a cooling H-bearing Earth's core could explain the seismologically observed velocity 182 anomalies at both the mantle and the core sides of the CMB, i.e., the CRZ and some ULVZs. Another 183 important implication is that the CRZ and some ULVZs from FeSi precipitation should be relatively young 184 structures, which may have existed only after the outermost core has cooled to a temperature below the 185 melting temperature of B2 FeSi. It is important to note that, however, Si and H are assumed to be the 186 major light elements and other candidate light elements, such as S, C or O, are not considered in our 187 experiments and models. Therefore, future studies should address these elements.

Some ocean island basalts are believed to be linked to the structures at the CMB through mantle plumes. 189 The tungsten isotope anomalies found in some ocean island basalts appear to be a core signature 12. 190 However, processes which can lead to the geochemical observation remain unclear. In order to fit a range 191 of geochemical constraints, a model involving core-mantle equilibrium has been proposed¹². If a core 192 material, such as FeSi, is mixed with mantle silicates to form some ULVZs, which are often inferred to be 193 the source region of the mantle plumes (and therefore volcanic rocks with deep origin)^{12,40}, a small-scale 194 localized equilibrium between the core and mantle materials in ULVZs may be established, providing a 195 viable source for the geochemical observation. Therefore, the FeSi crystallization in a H-bearing outer core provides a new process to explain both the geochemical and the geophysical observations at the CMB. 197

References

- 1. Garnero, E. J., Helmberger, D. V. & Grand, S. P. Constraining outermost core velocity with *SmKS* waves. *Geophys. Res. Lett.* **20**, 2463–2466 (1993).
- 201 2. Yu, S. & Garnero, E. J. Ultralow velocity zone locations: A global assessment. *Geochem. Geophys. Geosystems* 19, 396–414 (2018).
- 3. Rost, S. & Revenaugh, J. Seismic detection of rigid zones at the top of the core. *Science* **294**, 1911–1914 (2001).

- ²⁰⁵ **4.** Thorne, M. S. & Garnero, E. J. Inferences on ultralow-velocity zone structure from a global analysis of *SPdKS* waves. *J. Geophys. Res. Solid Earth* **109** (2004).
- 5. Knittle, E. & Jeanloz, R. Earth's core-mantle boundary: Results of experiments at high pressures and temperatures. *Science* **251**, 1438–1443 (1991).
- **6.** Dobson, D. P. & Brodholt, J. P. Subducted banded iron formations as a source of ultralow-velocity zones at the core–mantle boundary. *Nature* **434**, 371–374 (2005).
- 7. Mao, W. L. *et al.* Iron-rich post-perovskite and the origin of ultralow-velocity zones. *Science* **312**, 564–565 (2006).
- 8. Wicks, J. K., Jackson, J. M., Sturhahn, W. & Zhang, D. Sound velocity and density of magnesiowüstites: Implications for ultralow-velocity zone topography. *Geophys. Res. Lett.* 44, 2148–2158 (2017).
- 9. Liu, J. *et al.* Hydrogen-bearing iron peroxide and the origin of ultralow-velocity zones. *Nature* **551**, 494–497 (2017).
- 10. Mergner, V. *et al.* Sound velocities in FeSi at lower mantle conditions and the origin of ultralow-velocity zones. *Geophys. Res. Lett.* **48**, e2020GL092257 (2021).
- 11. Hirose, K., Wood, B. & Vočadlo, L. Light elements in the Earth's core. *Nat. Rev. Earth & Environ*. 1–14 (2021).
- Mundl-Petermeier, A. *et al.* Anomalous ¹⁸²W in high ³He/⁴He ocean island basalts: Fingerprints of Earth's core? *Geochimica et Cosmochimica Acta* **271**, 194–211 (2020).
- Williams, Q. & Garnero, E. J. Seismic evidence for partial melt at the base of Earth's mantle. *Science* 273, 1528–1530 (1996).
- 226 **14.** Buffett, B. A. Earth's core and the geodynamo. *Science* **288**, 2007–2012 (2000).
- 227 **15.** McDonough, W. F. & Sun, S.-S. The composition of the Earth. *Chem. geology* **120**, 223–253 (1995).
- 16. Fischer, R. A. *et al.* Equations of state in the Fe-FeSi system at high pressures and temperatures. *J. Geophys. Res. Solid Earth* 119, 2810–2827 (2014).
- ²³⁰ **17.** Pépin, C. M., Dewaele, A., Geneste, G., Loubeyre, P. & Mezouar, M. New iron hydrides under high pressure. *Phys. Rev. Lett.* **113**, 265504 (2014).
- **18.** Tagawa, S. *et al.* Experimental evidence for hydrogen incorporation into Earth's core. *Nat. Commun.* **12**, 1–8 (2021).
- ²³⁴ **19.** Tagawa, S., Ohta, K., Hirose, K., Kato, C. & Ohishi, Y. Compression of Fe–Si–H alloys to core pressures. *Geophys. Res. Lett.* **43**, 3686–3692 (2016).
- 20. Fu, S., Chariton, S., Prakapenka, V. B., Chizmeshya, A. & Shim, S.-H. Hydrogen solubility in fesi alloy phases at high pressures and temperatures. *Am. Mineral. J. Earth Planet. Mater.* **107**, 2307–2314 (2022).
- 239 **21.** Fu, S., Chariton, S., Prakapenka, V. B., Chizmeshya, A. & Shim, S.-H. Stable hexagonal ternary alloy phase in Fe-Si-H at 28.6–42.2 GPa and 3000 K. *Phys. Rev. B* **105**, 104111 (2022).
- 22. Hikosaka, K. *et al.* Melting phase relations in Fe–Si–H at high pressure and implications for Earth's inner core crystallization. *Sci. Reports* **12**, 1–8 (2022).
- 243 **23.** Ji, C. et al. Stability of Ar(H₂)₂ to 358 GPa. Proc. Natl. Acad. Sci. **114**, 3596–3600 (2017).

- 244 **24.** Kato, C. *et al.* Stability of fcc phase FeH to 137 GPa. *Am. Mineral. J. Earth Planet. Mater.* **105**, 917–921 (2020).
- 25. Hirao, N., Kondo, T., Ohtani, E., Takemura, K. & Kikegawa, T. Compression of iron hydride to 80 gpa and hydrogen in the earth's inner core. *Geophys. Res. Lett.* **31** (2004).
- 248 **26.** Thompson, E. *et al.* High-pressure geophysical properties of fcc phase FeH_x. *Geochem. Geophys. Geosystems* **19**, 305–314 (2018).
- 27. Ozawa, H., Hirose, K., Yonemitsu, K. & Ohishi, Y. High-pressure melting experiments on Fe–Si alloys and implications for silicon as a light element in the core. *Earth Planet. Sci. Lett.* **456**, 47–54 (2016).
- 28. Campbell, A. J., Seagle, C. T., Heinz, D. L., Shen, G. & Prakapenka, V. B. Partial melting in the iron–sulfur system at high pressure: A synchrotron x-ray diffraction study. *Phys. Earth Planet. Interiors* **162**, 119–128 (2007).
- 256 **29.** Lord, O. T. *et al.* The FeSi phase diagram to 150 GPa. *J. Geophys. Res. Solid Earth* **115** (2010).
- 30. Anzellini, S., Dewaele, A., Mezouar, M., Loubeyre, P. & Morard, G. Melting of iron at Earth's inner core boundary based on fast x-ray diffraction. *Science* 340, 464–466 (2013).
- 31. Hirose, K. *et al.* Hydrogen limits carbon in liquid iron. *Geophys. Res. Lett.* 46, 5190–5197 (2019).
- 260 **32.** Edmund, E. *et al.* The Fe-FeSi phase diagram at Mercury's core conditions. *Nat. Commun.* **13**, 1–9 (2022).
- Davies, C., Pozzo, M., Gubbins, D. & Alfe, D. Constraints from material properties on the dynamics and evolution of Earth's core. *Nat. Geosci.* **8**, 678–685 (2015).
- 264 **34.** Dewaele, A. *et al.* Quasihydrostatic equation of state of iron above 2 Mbar. *Phys. Rev. Lett.* **97**, 215504 (2006).
- 266 **35.** Dziewonski, A. M. & Anderson, D. L. Preliminary reference Earth model. *Phys. Earth Planet.*267 *Interiors* **25**, 297–356 (1981).
- **36.** Komabayashi, T. & Fei, Y. Internally consistent thermodynamic database for iron to the Earth's core conditions. *J. Geophys. Res. Solid Earth* **115** (2010).
- 37. Morard, G. *et al.* Fe–FeO and Fe–Fe₃C melting relations at Earth's core–mantle boundary conditions: Implications for a volatile-rich or oxygen-rich core. *Earth Planet. Sci. Lett.* **473**, 94–103 (2017).
- 38. Nakagawa, T. & Tackley, P. J. Influence of initial CMB temperature and other parameters on the thermal evolution of Earth's core resulting from thermochemical spherical mantle convection.

 Geochem. Geophys. Geosystems 11 (2010).
- Hernlund, J. W. & Jellinek, A. M. Dynamics and structure of a stirred partially molten ultralow-velocity zone. *Earth Planet. Sci. Lett.* **296**, 1–8 (2010).
- 40. Li, M., McNamara, A. K., Garnero, E. J. & Yu, S. Compositionally-distinct ultra-low velocity zones on Earth's core-mantle boundary. *Nat. Commun.* **8**, 1–9 (2017).

Methods

281

282

283

284

285

286

290

291

292

293

294

296

298

300

301

302

304

306

307

308

310

312

313

314

316

317

318

320

Experimental procedure The Fe-9wt%Si alloy starting material with 8.84 ± 0.30 wt% Si (Fe_{0.83}Si_{0.17}) was purchased from GoodFellow Corporation. Chemical analysis of the sample can be found in Ref.²¹. The analysis found that the Fe-9wt%Si sample is homogeneous. The powder with an average grain size of 3–5 μ m was compressed into less than 7– μ m thick foils and then loaded into DACs for high *P-T* experiments. Symmetric DACs with culet sizes between 200 μ m flat and 120 μ m beveled (300- μ m outer bevels) were used to pre-indent Re gaskets to a thickness of ~20 μ m. Holes with diameters of 60% of the culet sizes were drilled in the pre-indented areas to be used as sample chambers. We loaded small grains of the same starting materials on both sides of the diamond anvils to avoid direct contact with the foil²¹. This configuration allows for better thermal insulation and laser coupling during heating (Extended Data Figure 1). A piece of Au and ruby were placed close to the sample foil in the chamber as pressure calibrants^{41,42}.

High P-T heating experiments on Fe-9wt%Si with H were carried out at the 13-IDD beamline of the GeoSoilEnviroCARS (GSECARS) sector of the Advanced Photon Source (APS), Argonne National Laboratory (ANL). The infrared laser has a wavelength of 1064 nm and beams with flat-top intensity profiles ($\sim 15 \ \mu m$ in diameter) were focused on both sides of the sample for heating⁴³. An incident monochromatic X-ray beam with a wavelength of 0.3344 Å was focused to $3 \times 4 \mu m^2$ and aligned co-axially with the laser beam for XRD measurements. To achieve the pressure from mid-lower mantle to CMB, three DACs were prepared (Extended Data Table 1). For DAC #1, pure H₂ gas was loaded as a pressure medium and hydrogen source using a gas loading system at Arizona State University. Because pure H can fast diffuse into diamond anvils at high P-T, pulsed laser heating with a repetition rate of 10 kHz were employed for heating to sufficiently high temperatures²⁰. For DACs #2 and #3, an Ar-H₂ mixture containing 60-70% H₂ was loaded into the DACs for heating above 70 GPa. The Earth's core should have a finite amount of H as a light element, thus, Ar in the Ar-H₂ mixture reduces the H supply to the sample in our experiments. According to the Rietveld refinements on mole fraction of quenched products (Figure 1), such an experimental setup limits less than 1.7 wt% H in the metal alloys. Ar also reduces H diffusion to diamond anvils, enabling both continuous-wave and pulsed laser heating. For the continuous-wave laser heating, a heating duration of 2-5 min was conducted, which was sufficient for achieving near equilibrium conditions between melt and solid²¹.

The prepared DACs were first compressed to target pressures. Double-sided laser heating was employed to melt Fe-9wt%Si in H at high *P-T*. The thermal radiation spectra from both sides of the samples were measured and fit to a Plank function based on a gray-body approximation after correcting for the system response to obtain the temperatures of both sides⁴⁴. 2D XRD mappings were conducted on the heated spots at high pressures to determine the spatial distribution of phases after melting. XRD data were also collected during compression and decompression at the center of heated spots at room temperature (Extended Data Table 2). We calculated pressures and their uncertainties from the measured unit-cell volumes of Au before and after each laser heating. We note that Au was not mixed with the sample to prevent alloying between them. Because Au was not heated, we did not observe gold hydride and therefore the gold grains remained as a reliable internal pressure standard throughout the experiments (Extended Data Figure 2).

Data analysis We used DIOPTAS software⁴⁵ to integrate XRD images to patterns. PeakPo software⁴⁶ were employed to identify the diffraction peaks and to derive unit-cell parameters of the observed phases. The Pytheos toolset⁴⁷ was used to calculate pressures from the measured volumes of Au.

Estimation for H and Si contents in the quenched products We calculated volume differences between the observed alloys (B2, fcc, and dhcp phases) and their pure end members from previous experiments 16,34,48 . From the volume differences, we can then determine the Si and H contents in the phases (Extended Data Table 2). For H, studies have reported the equations of state of fcc and dhcp FeH_x (x = 1) 17,24 . Assuming a linear H effect on the volumes of fcc/dhcp FeH_x, its H content can be calculated as: $x = V_{\text{FeH}_x}/(V_{\text{FeH}} - V_{\text{Fe}})$, where V_{FeH_x} is the measured volume of fcc or dhcp FeH_x, and V_{FeH} and V_{Fe} are the volumes of pure FeH and Fe metal, respectively, at a given pressure 17,24 . For Si, a recent study determined the effect of Si on the thermal equation of state of B2 Fe-Si alloys together with previous experimental data on the FeSi end member 16 . Following a similar procedure as the H case, we can estimate the Si deviations from Fe/Si=1:1 in the B2 structure of FeSi alloy. The uncertainties in our measured volumes are less than 1%. Based on error propagation, the estimated uncertainty for Si and H contents from this method is 2–5%.

Estimation of the bulk composition of our Fe-Si-H The phase fractions of the quenched products can be obtained from Rietveld refinements of the XRD patterns measured after heating at high pressures (Figure 1). Combined with the estimated Si and H contents discussed above, the phase fraction allows us to calculate the bulk chemical composition of the Fe-Si-H system in this study. Calculations show that our Fe-Si-H system contains 91.2 wt% Fe, 7.4 wt% Si, and 1.4 wt% H at 49.5 GPa and 121.6 GPa; and 92.3 wt% Fe, 6.0 wt% Si, and 1.7 wt% H at 85.8 GPa.

Estimation of the amount of Si to crystallize out in the outermost core to explain the CRZ or the ULVZs For a global FeSi layer with a thickness of d_{CRZ} (in km) formed from the FeSi precipitation at the outermost region (d_{PCL} in km) of the outer core, a mass balance yields:

$$\frac{4}{3}\pi \left[r_{\text{CMB}}^{3} - (r_{\text{CMB}} - d_{\text{CRZ}})^{3} \right] \cdot \rho_{\text{FeSi}} = \frac{4}{3}\pi \left[r_{\text{CMB}}^{3} - (r_{\text{CMB}} - d_{\text{PCL}})^{3} \right] \cdot \rho_{\text{OC}} \cdot x \cdot \frac{M_{\text{Fe}} + M_{\text{Si}}}{M_{\text{Si}}}$$
(1)

where x is the Si loss (in weight fraction) by the precipitation, r_{CMB} is the radius at the core-mantle boundary (3481 km), ρ_{FeSi} is the density of B2 FeSi at the CMB relevant P-T conditions (\sim 8.47 g/cm³)¹⁶, ρ_{OC} is the density of liquid outer core (e.g., \sim 9.90 g/cm³ near the CMB from the PREM model³⁵), and M_{Fe} and M_{Si} are the molar masses of Fe and Si, respectively. If we assume that the global CRZ is 100-m thin ($d_{\text{CRZ}} = 0.1$ km) and the thicknesses of the outermost core layer where FeSi precipitates is 40 km ($d_{\text{PCL}} = 40$ km), the Si loss by precipitation in the layer (x) is 0.07 wt%. With the further cooling of the Earth's core (therefore, a decrease in temperature), d_{PCL} increases and the required Si loss in the region will decrease accordingly. If the outer core is well mixed over geological time, the Si loss of the entire outer core is less than 0.003 wt%.

Following a similar procedure for ULVZs, the Si loss (x in weight fraction) in the outermost core by the FeSi precipitation can be estimated as:

$$\frac{4}{3}\pi \left[(r_{\text{CMB}} + d_{\text{ULVZ}})^3 - r_{\text{CMB}}^3 \right] \cdot S \cdot V \cdot \rho_{\text{FeSi}} = \frac{4}{3}\pi \left[r_{\text{CMB}}^3 - (r_{\text{CMB}} - d_{\text{PCL}})^3) \right] \cdot \rho_{\text{OC}} \cdot x \cdot \frac{M_{\text{Fe}} + M_{\text{Si}}}{M_{\text{Si}}}$$
(2)

where $d_{\rm ULVZ}$ is the average thickness of ULVZs, S is the area fraction of ULVZs at the CMB ($\sim 10.3\%$)², and V is the volume fraction of FeSi in ULVZs ($\sim 8.4\%$) to account for the seismologically observed density and velocities¹⁰. For $d_{\rm ULVZ}$ =10–30 km and $d_{\rm PCL}$ =40 km, x is 0.06–0.18 wt%. If the outer core is completely homogenized, the Si loss of the whole outer core is 0.003–0.009 wt%. Therefore, the Si loss is minimal.

References

- 41. Ye, Y., Shim, S.-H., Prakapenka, V. & Meng, Y. Equation of state of solid Ne inter-calibrated with the MgO, Au, Pt, NaCl-B2, and ruby pressure scales up to 130 GPa. *High Press. Res.* 38, 377–395 (2018).
- Shen, G. *et al.* Toward an international practical pressure scale: A proposal for an ipps ruby gauge (ipps-ruby2020). *High Press. Res.* **40**, 299–314 (2020).
- 43. Goncharov, A. F. *et al.* X-ray diffraction in the pulsed laser heated diamond anvil cell. *Rev. Sci. Instruments* 81, 113902 (2010).
- ³⁶⁷ **44.** Prakapenka, V. *et al.* Advanced flat top laser heating system for high pressure research at gsecars: application to the melting behavior of germanium. *High Press. Res.* **28**, 225–235 (2008).
- ³⁶⁹ **45.** Prescher, C. & Prakapenka, V. B. Dioptas: a program for reduction of two-dimensional x-ray diffraction data and data exploration. *High Press. Res.* **35**, 223–230 (2015).
- 46. Shim, S. PeakPo a python software for x-ray diffraction analysis at high pressure and high temperature. *Zenodo: Meyrin, Switz.* (2017).
- 373 **47.** Shim, S. Pytheos-a python tool set for equations of state pytheos-a python tool set for equations of state. *URL https://doi. org/10.5281/zenodo* **802392** (2017).
- ³⁷⁵ **48.** Dorogokupets, P., Dymshits, A., Litasov, K. & Sokolova, T. Thermodynamics and equations of state of iron to 350 gpa and 6000 k. *Sci. reports* **7**, 1–11 (2017).
- 49. Yokoo, S. *et al.* Composition-dependent thermal equation of state of B2 Fe-Si alloys at high pressure.

 Am. Mineral. https://doi.org/10.2138/am-2022-8067 (2022, in press).

379 Acknowledgments

The authors thank E. J. Garnero and M. Li for discussion. This work is supported by NSF-Astronomical Science (AST200567) and NSF-Earth Science (EAR1921298). We acknowledge the support of GeoSoilEnviroCARS (University of Chicago, Sector 13) for synchrotron experiments. GeoSoilEnviroCARS was supported by the National Science Foundation - Earth Sciences (EAR-1634415). This research used resources of the Advanced Photon Source, a U.S. Department of Energy (DOE) Office of Science User Facility operated for the DOE Office of Science by Argonne National Laboratory under Contract No. DE-AC02-06CH11357.

387 Author contributions statement

S.F. and S.H.S. conceived the project, S.F., S.C., V.B.P., and S.H.S. conducted synchrotron experiments, S.F. analysed the results, S.F. and S.H.S. wrote the manuscript. All authors reviewed the manuscript.

Additional information

The authors declare no conflict of interests.

Materials & Correspondence

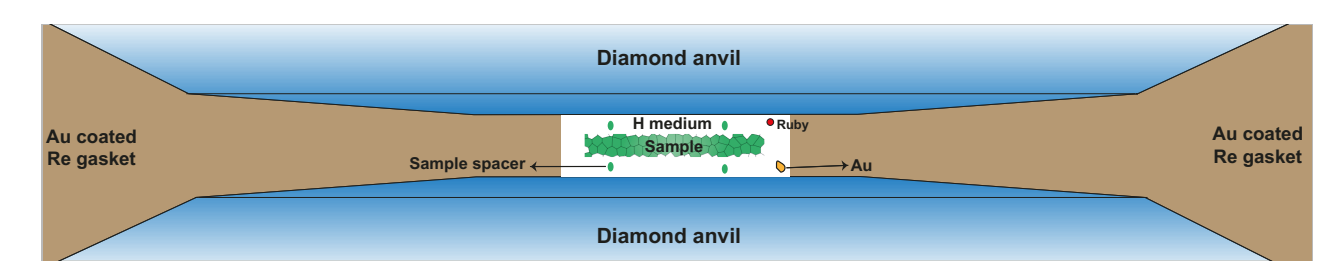
Correspondence and requests for materials should be addressed to S.F (fsyxhy@gmail.com) or S.H.S (sshim5@asu.edu).

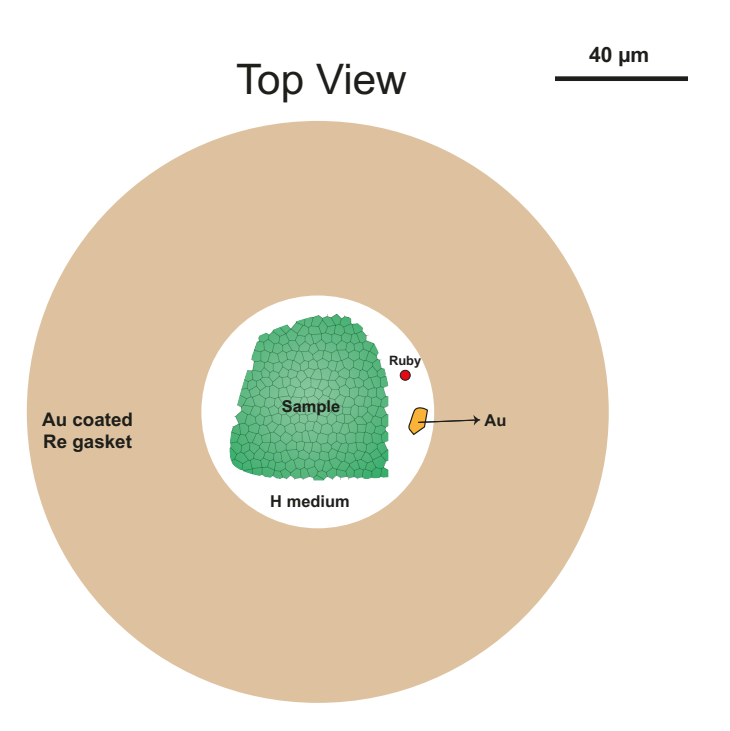
1 Supplementary Information

396 Hexagonal-close packed (hcp) phase observed after laser heating

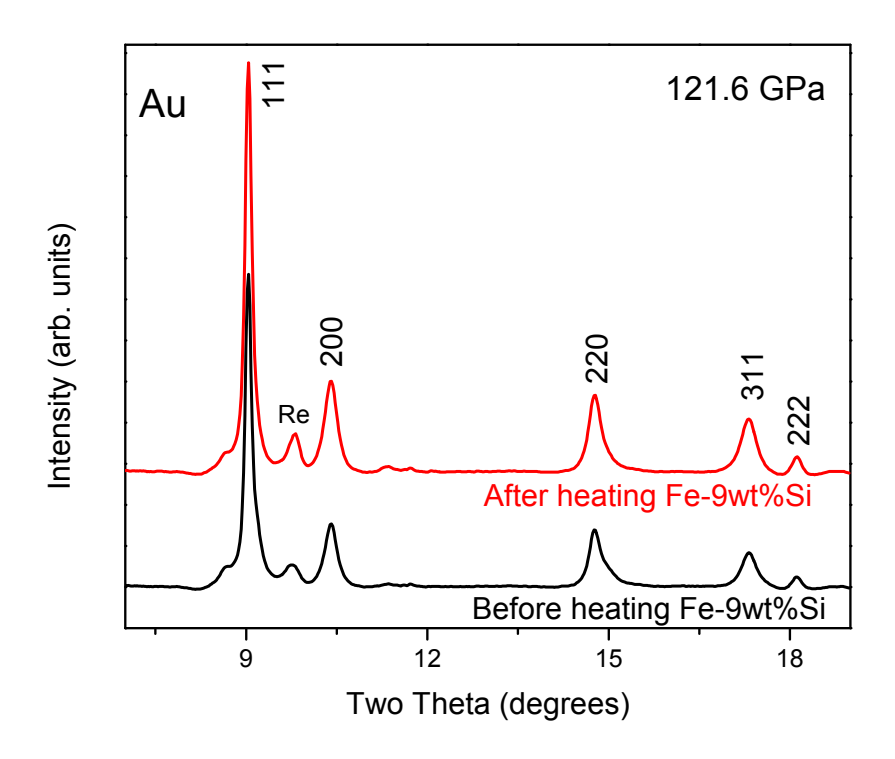
The volume of the hcp phase is consistent with that of the H-free Fe-9wt%Si alloy below \sim 80 GPa and 397 gradually increases at higher pressures (Extended Data Figure 4b). Both Si and H can increase the volume 398 of hcp Fe-Si-H alloys 16,17. Estimations show that the hcp phase could have a range of compositions: 399 $\text{Fe}_{0.83\pm\delta}\text{Si}_{\mp\delta}\text{H}_x$ ($\delta < 0.1$ and x < 0.21). It is difficult to determine whether the hcp phase is the product or remnant of the starting materials. Because the hcp phase is shown to have weak diffraction peaks in the 401 patterns and therefore its small amount (Figure 1), it does not affect our main findings on the formation of B2 $Fe_{1\pm\delta}Si_{1\pm\delta}$ and FeH_x as major phases in the heated spots. We note that the Fe-Si alloys became 403 fragile after heating to high temperatures in a H medium in LHDACs, which made it difficult to recover 404 the sample for chemical analyses. 405

Side View

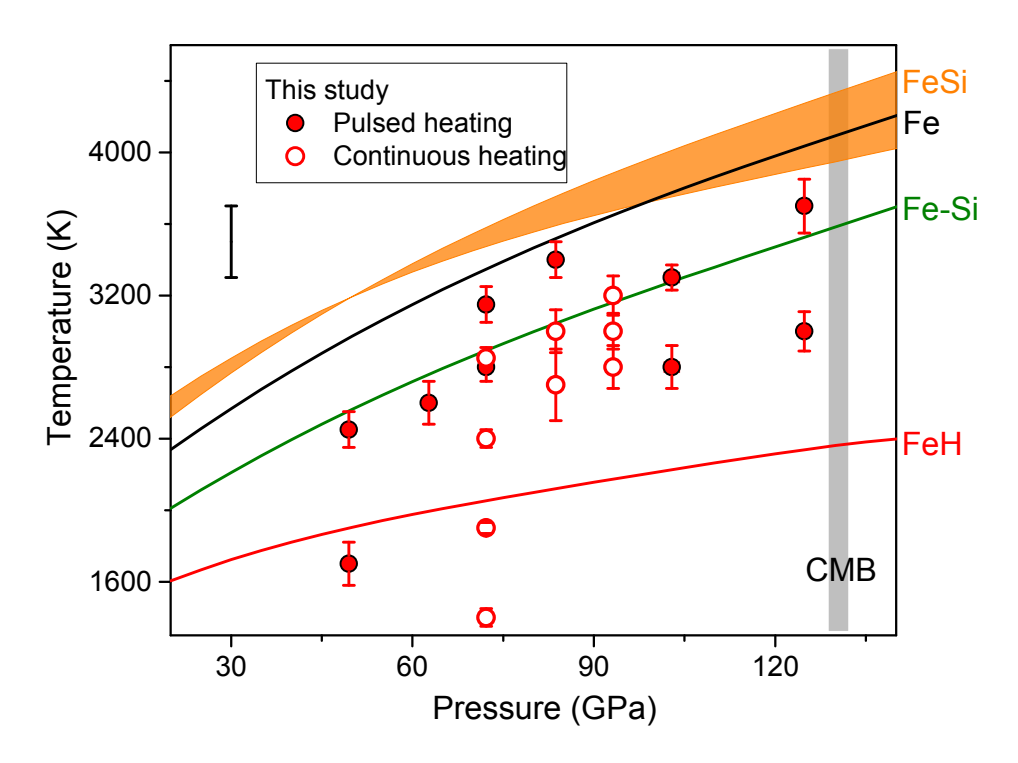




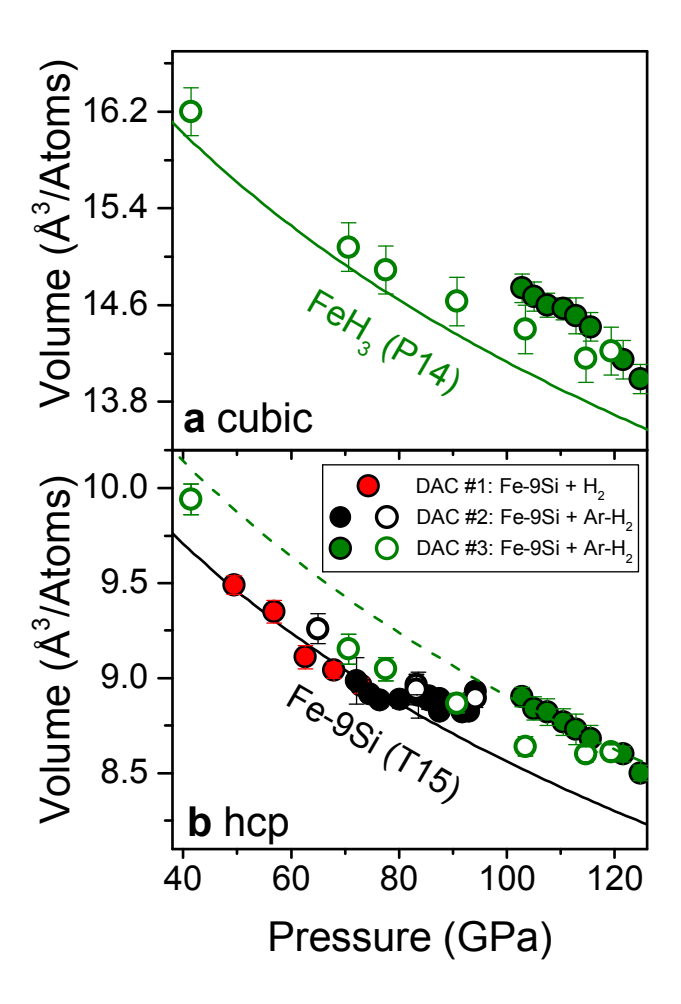
Extended Data Fig. 1. Schematic diagrams of the experimental setup used in this study. Top and bottom figures show side and top views, respectively, of a DAC loaded with the Fe-9wt%Si alloy foil in the presence of H as a medium. Beveled diamonds with a 120- μ m inner culet and 300- μ m outer bevel were used for the experiments over 100 GPa. The initial thickness of the compressed foil is less than 7 μ m. In this setup, the loaded H can penetrate the compressed sample foil and exist between the grain boundaries.



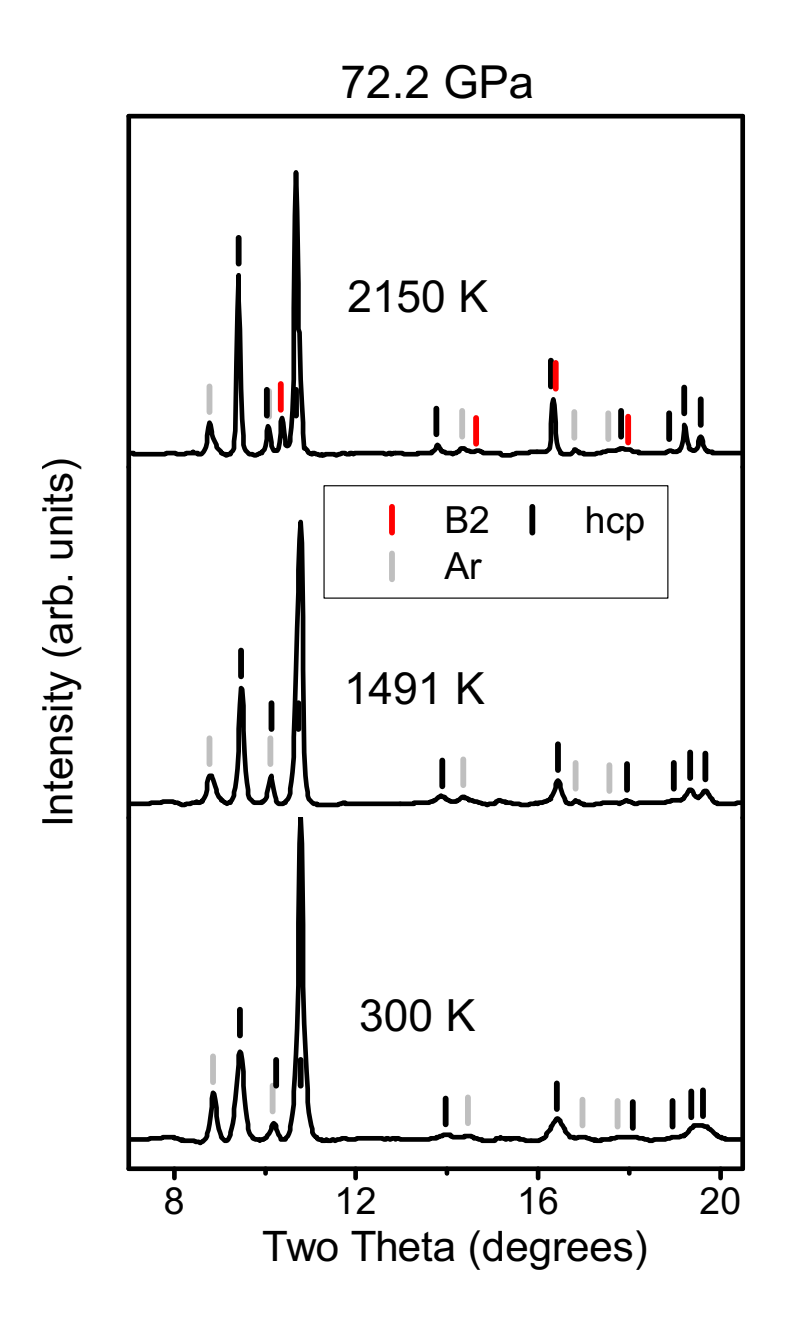
Extended Data Fig. 2. Representative X-ray diffraction patterns of Au loaded for a pressure standard. We provided patterns measured before and after laser-heating the Fe-9wt%Si alloy in a H-bearing medium at 121.6 GPa. The Miller indices of Au were provided, and "Re" denotes weak peaks from the gasket. The gold was intentionally loaded near the gasket inside the sample chamber to avoid direct contact with the sample foil. Because of the setup, the grain is close to the gasket, which can result in detection of weak diffraction lines from the Re gasket. Au was not heated in our experiments. The Au diffraction peaks do not show any changes before and after heating the sample and we did not find any sign of hydrogenation of gold. The wavelength of the incident X-ray beam is 0.3344 Å.



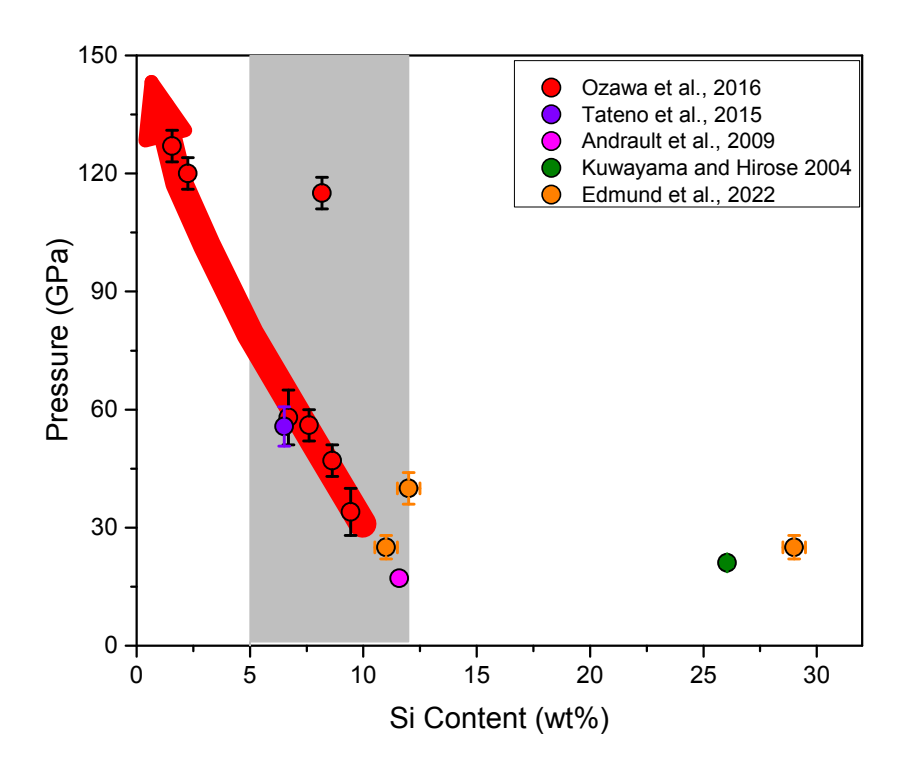
Extended Data Fig. 3. Pressure–temperature conditions of our experiments. The solid and open circles represent pulsed and continuous heating runs, respectively. Melting curves of the related alloy phases are shown: Fe metal (black)³⁰, Fe-Si alloys containing 7-22 wt% Si (olive)³², FeSi (shaded orange area)²⁹, and FeH (red)³¹. The error bar is the representative uncertainty for the experimental melting curves.



Extended Data Fig. 4. Pressure-volume relationship of **a** cubic FeH₃ and **b** the hcp phase observed after laser heating at 300 K. The red, black, and olive circles are from DACs #1, #2, and #3, respectively. The solid and open circles are measured volumes during compression and decompression, respectively. The FeH₃ appeared only after heating above 100 GPa. Previous experimental data on pure FeH₃ (P14)¹⁷ and H-free Fe-9wt%Si (T15)⁵⁰ were plotted as solid lines for comparison. The dashed line in **b** is the best fit for the compression data of the hcp phase in DAC #3, which has a 4–5% higher volume than H-free Fe-9wt%Si (see Extended Data Table 2).



Extended Data Fig. 5. X-ray diffraction patterns measured during heating Fe-9wt%Si in a H-bearing medium at 72.2 GPa. At temperatures below 1491 K, no melting was observed. At 2150 K, the Si-rich (Si/Fe \approx 1) B2 phase appears. The vertical ticks indicate peak positions of the identified phases. The wavelength of incident X-ray beam is 0.3344 Å.



Extended Data Fig. 6. Si content of the eutectic liquid in an Fe-FeSi binary. The figure is revised from Ref.²⁷. Data are from Refs.^{27,32,50–52}. The large red arrow highlights that the Si content in the eutectic liquid composition of a H-free Fe-Si system decreases with pressure. The gray band shows the expected Si content for the Earth's outer core.

Extended Data Table 1. Experimental conditions of the DAC runs for Fe-9wt%Si in a H-bearing medium. Note that the pressures reported here were measured at room temperature. Temperatures were gradually increased in the experiments and we presented the highest temperature achieved in the runs. The 1σ uncertainties on the last digits are shown in parentheses.

	Medium	Heating technique	Pressure (GPa)	Temperature (K)
DAC #1	Duna II	Pulsed	49.5(6)	2450(100)
	Pure H ₂	Puised	62.7(5)	2600(120)
DAC #2	Ar-H ₂ mixture		72.2(7)	3150(100)
		Pulsed and continuous	83.7(7)	3400(100)
			93.2(8)	3000(110)
DAC #3	Ar-H ₂ mixture	Pulsed	102.9(13)	3300(120)
	Ai-112 Illixtuic	i uiscu	124.8(9)	3700(150)

Extended Data Table 2. Unit-cell volumes of the phases observed after laser heating at high pressures. These data points were measured during compression and/or decompression at 300 K. The 1σ uncertainties on the last digit(s) are shown in parentheses.

<i>P</i> (GPa)	a(Au) (Å)	B2 Fe _{1-δ}	$Si_{1+\delta}$			FeH _x			Fe _{0.83±δ} S	$5i_{0.17 \pm \delta}H_x$	FeH ₃
P (GPa)	a(Au)(A)	a(B2) (Å)	δ	a(fcc) (Å)	х	a(dhcp) (Å)	c(dhcp) (Å)	x	a(hcp) (Å)	c(hcp) (Å)	<i>a</i> (Å)
DAC #1: Fe-9wt%Si heated in a pure H ₂ medium											
Heated at 49.5 GPa up to 2450 \hat{K} , compression											
49.5(6)	3.844(3)	2.624(1)	0.04	3.549(6)	1.08(1)	2.515(3)	8.152(9)	1.02(2)	2.384(1)	3.857(3)	-
56.8(13)	3.822(6)	2.608(3)	0.05	3.527(9)	1.04(2)	2.509(6)	8.135(15)	1.00(3)	2.373(3)	3.838(5)	-
Heated at 62.7 GPa up to 2600 K, compression											
62.7(5)	3.806(2)	2.597(3)	0.04	3.512(9)	1.04(2)	2.475(6)	8.110(12)	1.02(3)	2.351(2)	3.804(5)	-
68.0(4)	3.793(2)	2.586(1)	0.04	3.507(7)	1.09(3)	2.450(5)	8.115(12)	0.98(2)	2.346(2)	3.795(6)	-
73.0(15)	3.780(6)	2.584(2)	0.02	3.477(7)	1.00(2)	2.441(4)	8.072(14)	0.98(3)	2.338(2)	3.783(7)	-
				DAC #2: Fe-9	wt%Si h	eated in a Ar-	H ₂ mixture m	edium			
Heated at 72.2 GPa up to 3150 K, compression											
72.2(7)	3.783(2)	2.588(1)	0.01	3.479(2)	1.01(1)	2.453(3)	7.875(12)	0.87(3)	2.352(2)	3.743(2)	_
74.6(6)	3.777(1)	2.583(1)	0.01	3.464(2)	0.96(1)	2.450(1)	7.786(13)	0.84(2)	2.351(1)	3.723(2)	_
76.5(7)	3.773(2)	2.579(1)	0.02	3.459(2)	0.96(2)	2.443(4)	7.792(22)	0.84(3)	2.349(1)	3.709(1)	_
80.1(7)	3.764(2)	2.572(2)	0.02	3.450(2)	0.96(2)	2.418(7)	7.872(18)	0.82(4)	2.352(4)	3.709(8)	_
83.5(7)	3.757(2)	2.570(1)	0.01	3.444(1)	0.97(2)	2.414(7)	7.873(15)	0.83(4)	2.357(8)	3.705(17)	_
00.10(,)	(-)	,			. ,		K, compression		=100.(0)		
83.7(7)	3.757(2)	2.566(1)	0.02	3.455(3)	1.04(2)	2.441(1)	7.776(9)	0.90(5)	2.355(5)	3.716(11)	_
85.5(8)	3.753(2)	2.569(1)	-0.01	3.439(3)	0.97(2)	2.410(4)	7.953(8)	0.90(5)	2.354(1)	3.710(3)	_
87.5(9)	3.748(2)	2.563(2)	-0.04	3.447(1)	1.05(3)	2.414(4)	7.974(16)	0.95(3)	2.352(4)	3.711(7)	_
91.7(9)	3.740(2)	2.561(2)	-0.01	3.440(1)	0.99(1)	2.411(3)	7.954(9)	0.93(2)	2.347(9)	3.699(6)	_
93.0(9)	3.737(2)	2.556(1)	0.01	3.435(1)	1.04(1)	2.407(3)	7.992(11)	0.97(2)	2.348(1)	3.695(1)	_
22.0(2)	3.737(2)	2.330(1)	0.01		\ /		, decompression		2.3 10(1)	3.073(1)	
93.2(8)	3.737(2)	2.555(1)	0.03	3.417(1)	1.02(1)	2.400(1)	7.958(8)	0.99(2)	2.344(1)	3.731(5)	_
94.2(9)	3.735(2)	2.561(1)	-0.02	3.431(3)	0.99(2)	2.100(1)	-	-	2.353(2)	3.724(8)	_
83.2(9)	3.757(3)	2.568(2)	0.03	3.448(4)	0.96(1)	2.406(1)	7.919(9)	0.82(3)	2.355(2)	3.732(9)	_
65.0(8)	3.800(4)	2.592(2)	0.05	3.485(2)	0.94(3)	2.400(1)	7.515(5)	-	2.383(1)	3.763(9)	_
	3.000(1)	2.372(2)			\ /	eated in a Ar.	H ₂ mixture m	edium	2.303(1)	3.763())	
							K, compressio				
102.9(13)	3.718(3)	2.554(1)	-0.05	-	-	2.413(5)	7.859(13)	1.07(5)	2.334(2)	3.775(6)	2.452(7)
105.1(11)	3.714(2)	2.553(1)	-0.05	_	_	2.415(3)	7.861(18)	1.06(2)	2.333(2)	3.752(8)	2.448(7)
107.5(11)	3.709(2)	2.551(1)	-0.05	_	_	2.400(8)	7.903(18)	1.07(1)	2.331(4)	3.748(9)	2.444(6)
110.5(12)	3.704(2)	2.551(1)	-0.05	_	_	2.400(0)	7.505(10)	-	2.327(4)	3.742(8)	2.442(5)
110.3(12)	3.700(2)	2.543(2)	-0.06	_	_	2.409(9)	7.810(22)	1.12(3)	2.324(5)	3.734(11)	2.439(8)
115.5(13)	3.695(3)	2.538(1)	-0.05		_	2.405(9)	7.782(19)	1.12(3)	2.320(4)	3.726(10)	2.434(7)
121.6(17)	3.685(4)	2.539(1)	-0.05	_	_	2.383(7)	7.778(15)	1.06(3)	2.312(3)	3.726(10)	2.419(9)
121.0(17)	3.063(4)	2.339(2)	-0.03	Heated at	124 8 GE		ζ, decompressi		2.312(3)	3.713(7)	2.419(9)
124.8(9)	3.680(2)	2.526(1)	-0.08	Ticated at	124.0 OI	2.379(3)	7.667(13)	0.98(1)	2.289(2)	3.748(6)	2.410(7)
119.4(8)	3.689(1)	2.533(1)	-0.06	-	-	2.379(3)	7.806(13)	0.98(1)	2.289(2)	3.746(6)	2.410(7)
119.4(8)	3.697(1)	2.539(1)	-0.05	-	-	2.370(3)	7.800(13)	1.14(5)	2.312(2) 2.298(2)	3.761(7)	2.423(4)
103.4(7)	3.717(1)	2.553(1)	-0.05	-	-	2.389(3)	7.916(14)	1.14(5)	2.298(2) 2.307(2)	3.744(6)	2.419(3)
90.7(8)	3.742(1)	2.566(2)	-0.03	-	-	2.400(3)	7.933(12)	0.98(3)	2.307(2)	3.744(0)	2.433(4)
. ,	3.742(1) 3.770(1)	2.586(2)	-0.03	-	-	· /	7.847(13) 7.874(16)	0.98(3)	2.340(3)	3.793(8) 3.816(9)	2.440(3)
77.5(8) 70.7(5)	3.786(1)	2.586(2) 2.601(2)	-0.05	-	-	2.453(7) 2.485(6)	7.874(16) 7.680(21)	0.95(2)	2.340(3)	3.866(12)	2.460(3)
				-			. ,				
41.4(8)	3.870(2)	2.668(2)	-0.07	-	-	2.518(9)	7.985(17)	0.89(5)	2.411(4)	3.948(9)	2.530(3)

06 References

- 50. Tateno, S., Kuwayama, Y., Hirose, K. & Ohishi, Y. The structure of Fe–Si alloy in Earth's inner core. Earth Planet. Sci. Lett. 418, 11–19 (2015).
- 51. Andrault, D. *et al.* Melting diagrams of Fe-rich alloys determined from synchrotron in situ measurements in the 15–23 GPa pressure range. *Phys. Earth Planet. Interiors* **174**, 181–191 (2009).
- 52. Kuwayama, Y. & Hirose, K. Phase relations in the system Fe-FeSi at 21 GPa. *Am. Mineral.* **89**, 273–276 (2004).